Numerical study of fiber deposition in airway replica using CFD-DEM simulation

Miloslav Belka[1,*], *Frantisek* Lizal[1], *Jakub* Elcner[1], *Ondrej* Misik[1] and *Miroslav* Jicha[1]

[1]Brno University of Technology, Department of thermodynamics and environmental sciences, 616 69 Brno, Czech Republic

Abstract. Inhalation of fibers has been a health concern for several decades. Although the use of some fibers, such as asbestos, was banned altogether in many countries, global demand for other fibers, such as man-made vitreous or carbon fibers, increases every year. The health hazard of fibers is given by their ability to penetrate deep into human lungs and avoid defensive mechanisms. This is mainly given by their anisometric shape and complex behavior in fluid flow, e.g. drag force acting on a fiber depends significantly on fiber orientation. The objective of the present work was to numerically investigate fiber transport and deposition in the model of child respiratory airways including the upper respiratory tract and tracheobronchial tree down to 2nd generation of branching. Computational fluid dynamics–discrete element method was employed to model a fiber motion during which the drag force was calculated based on actual fiber orientation in a flow. This method was compared to a simpler approach in which a modified drag coefficient accounting for fiber non-spherical shape was used. The results of the employed methods were compared.

1. Introduction

Fiber inhalation and deposition have gained a lot of attention due to the proven adverse effects of asbestos fibers. This is caused by both their aerodynamic properties and bio-persistence. Due to their shape, fibers tend to avoid deposition in upper respiratory airways and penetrate into lower airways more easily compared to spherical particles having the same aerodynamic diameter [1]. Once they deposit, they are able to resist pulmonary defense mechanisms and cause a bioactive response which plays an important role in the development of respiratory diseases, such as fibrosis, mesothelioma or lung cancer [2].

Although the use of asbestos has been banned in EU countries in 2005 [3], the asbestos exposure remains a hazard due to its release during the reconstruction or demolition of old buildings [4], Moreover, other fibrous materials raised concern about their potential inhalation toxicity similar to asbestos [5]. The ban on asbestos resulted in increased global demand for substitute construction materials, such as man-made vitreous fibers. The ongoing research in nanomaterials has brought promising materials, such as carbon nanotubes, that are produced on a large scale for industrial applications [6,7].

It is essential to provide information on lung deposition, among other things, to evaluate the toxicity of widely used or newly emerging materials to recommend exposure limits. As the *in vivo* measurements using human volunteers are out of the question because of ethical reasons, the use of physical replicas or computational models is the only viable option [8]. Experimental works on the deposition of glass, carbon, or asbestos fibers using airway casts have been carried out by some research groups [1,9,10]. However, this approach is tedious, expensive and time demanding as one has to rinse the deposited fibers from the casts and analyze the resulting samples manually [11].

Computational fluid and particle dynamics (CFPD) is more time and cost-effective compared to experiments. However, the fiber motion is complex due to its anisotropic shape and complicated underlying physics, e.g. the drag force depends on actual fiber orientation and fiber rotation must be considered [12]. The simplest approach to characterize the fiber motion is to employ equivalent sphere models, such as equivalent volume diameter [13]. Another method is to apply empirical equations for drag coefficients that take into consideration the non-spherical shape [14], such as [15]. These approaches are computationally less taxing, however, they ignore the actual fiber volume and orientation and assume that forces are applied to the particle center of gravity [16].

A more accurate but computationally demanding approach is to employ an Euler-Lagrange method enhanced by Euler's rotation equations that allows simulation of coupled translational and rotational fiber motion. This model was developed by [17] and later used by the same group to study asbestos fiber deposition in an idealized model of the upper tracheobronchial tree [13]. The model was implemented also by other researchers to predict deposition in realistic lung geometries of carbon [12] and unit-density fibers [18].

The aforementioned studies investigated fiber deposition using various techniques in idealized or realistic models of adults. However, inhalation

* Corresponding author: belka@fme.vutbr.cz

toxicological hazards concern also the youth population whose lung geometry and respiratory patterns vary from those of adults. Moreover, all the numerical studies have assumed that fibers stick to the wall after deposition as the respiratory walls are covered by mucus. This may not be true in all cases as the elastic force depends on the fiber orientation during a collision with the wall and fiber may bounce off the wall [19].

In this study, carbon and glass fiber deposition in a realistic replica of 5-year-old child was investigated. The fiber motion was described by both simple models utilizing equivalent diameters and a meshless discrete element method (DEM) that included equations for fiber torque and drag. Moreover, DEM accounts for both actual fiber orientation calculation and fiber-wall interactions that could lead to proper fiber deposition predictions.

2. Material and methods

2.1. Lung geometry

A realistic replica of a 5-year-old child respiratory airways was employed in the simulations. It included upper respiratory airways and the first two generations of tracheobronchial branching (Fig. 1). The geometry was developed by downscaling an adult geometry free of pathological alterations [20]. The scaling factors were calculated based on available data from pediatric respiratory airway measurements. As there are no studies that would include data on both upper and lower respiratory airways, two scaling factors were employed. The upper respiratory tract was down-scaled based on the length from the nostrils to the end of septum with a scaling factor of 0.54 [21]. The tracheobronchial tree was down-scaled with a scaling factor of 0.8 using a trachea length measured in [22]. Cylindrical parts were added to the oral cavity and lobe outlets to assure a developed flow profile at the inlets and to eliminate backflow at the outlets.

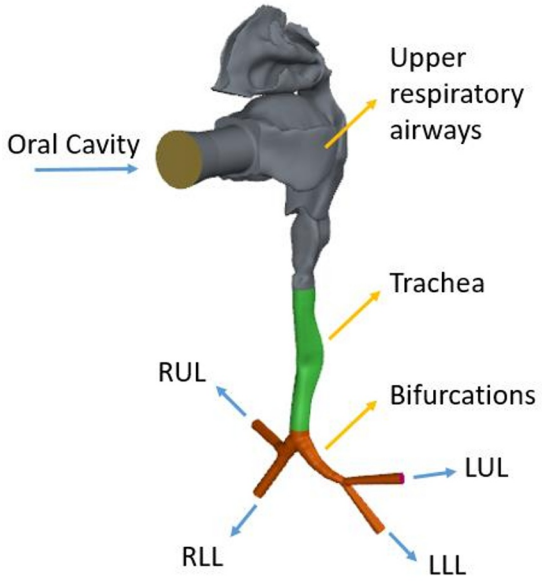

Fig. 1. Child digital replica of respiratory airways (LUL – left upper lobe, LLL – left lower lobe, RUL – right upper lobe, RLL – right lower lobe).

2.2. Numerical flow simulations

The digital replica was imported into a commercial solver Fluent (version 2022 R2, part of ANSYS 2022 R2 software). A computational grid containing 563278 polyhedral cells was generated. Prism cells were created at the replica walls to accurately resolve velocity gradients. The grid was chosen based on a grid sensitivity study as a compromise between accuracy and computational demands. The thickness of the first cell at the wall was determined in such a way that it satisfied $Y+ < 1$ condition.

The flow through the airway replica was solved using a k–ω SST turbulence model. This model proved to capture mean-flow dynamics reliably compared to Large eddy simulations while being computationally less demanding [23]. The scheme for pressure-velocity coupling was SIMPLE. Spatial discretization was of the second order.

Human breathing is realized by the acting of respiratory muscles that create an under-pressure inside the lungs and air is sucked in. Therefore, a zero gauge–pressure boundary condition was prescribed at the oral cavity entrance and outward pointing velocities were set at the lobe outlets in conformity with reality. The no-slip condition was assumed at the walls. The value of turbulent intensity at the oral cavity entrance was set to 5 % and the value of the ratio of turbulent viscosity to laminar viscosity was 10 %.

The fiber deposition was investigated for oral stationary inhalation with a flow rate of 12.5 L/min [24]. The flow rate division into different respiratory lobes can be found in Table 1 together with breathing regime parameters.

Table 1. Breathing regime and calculated flow rates through airway replica.

	lobar flow rate	tidal volume	respiratory rate
	L/min	L	brpm
LUL	3.16	0.21	25
LLL	2.58		
RUL	2.61		
RLL	4.15		
total	12.5		

2.3. Fiber motion simulations

Fiber deposition was investigated for two fiber types, carbon and glass fibers. Carbon fiber properties were adopted from [25]. The carbon fiber diameter was 3.6 μm and the aspect ratio (AR), i.e. ratio of fiber length to its diameter, was 30. The glass fiber properties were adopted from [1]. The glass fiber diameter was 1 μm and AR was 20. The density of carbon and glass fiber was 1830 and 2560 kg/m^3, respectively.

Lagrangian method

The fibers were tracked through the airway replica using a Lagrangian method and DEM. The lagrangian method was used in Fluent 2022 R2 and it means that the force balance equation was solved for every particle:

$$m_p \frac{d\vec{u}_p}{dt} = m_p \frac{\vec{u} - \vec{u}_p}{\tau_r} + m_p \frac{\vec{g}(\rho_p - \rho)}{\rho_p} \quad (1)$$

where m_p is particle mass, u_p is particle velocity, u denotes gas velocity, τ_r is particle relaxation time, g is gravitational acceleration, ρ_p denotes particle density, and ρ is gas density. The first term on the right side represents a drag force and the second term denotes a gravity and a lift force. Other forces acting on the particle were neglected. The particle relaxation time can be calculated using equation 2:

$$\tau_r = \frac{\rho_p d_p^2}{18\mu} \frac{24}{C_D Re} \quad (2)$$

where d_p is particle diameter, μ is gas dynamic viscosity, C_D is drag coefficient, and Re denotes particle Reynolds number. Particle Reynolds number is calculated using equation 3:

$$Re = \frac{\rho d_p |\vec{u}_p - \vec{u}|}{\mu} \quad (3)$$

The simplest and least accurate approach was to approximate fiber with a spherical particle having the same volume. In that case, d_p in equations 2 and 3 was substituted by volume equivalent diameter d_{ve}. The volume equivalent diameter of carbon and glass fibers was 12.8 and 3.1 μm, respectively. C_D for smooth spherical particles given by [26] was employed:

$$C_D = a_1 + \frac{a_2}{Re} + \frac{a_3}{Re} \quad (4)$$

where a_1, a_2, and a_3 are constants applied over several ranges of Re. The more appropriate approach was to use volume equivalent diameter together with the empirical correlation of C_d for non-spherical particles, such as the one from Haider and Levenspiel (H-L) [15]:

$$C_D = \frac{24}{Re}(1 + b_1 \cdot Re^{b_2}) + \frac{b_3 \cdot Re}{b_4 + Re} \quad (5)$$

where b_1, b_2, b_3, and b_4 are functions of sphericity, i.e. a ratio of a fiber surface area to a surface area of a sphere having the same volume.

10^4 particles were injected in each simulation from a circular injector located 5 mm upstream of the inlet. The injector diameter was set to 10 mm (the cylindrical inlet was 16 mm) in order to avoid deposition close to the injector. One-way coupling was employed as the fiber concentration was low and their effect on flow was neglected. The fibers were assumed as deposited when they touched the airway model walls.

DEM

DEM was employed using Rocky DEM (version 2022 R2, part of Ansys software 2022 R2). As DEM tracks only particles in meshless geometry, the calculated fluid flow was imported from Fluent to account for the effects of flow on the fibers. One–way coupling was employed. The particles were tracked in a similar way as in the Lagrangian method, but the force balance in equation 1 included also contact force F_c accounting for particle-particle and particle-wall interactions. DEM solved also particle rotation using the equation :

$$J_p \frac{d\omega_p}{dt} = M_c + M_D \quad (6)$$

where J_p is particle moment of inertia tensor, M_c denotes net torque generated by tangential forces, and M_D is the torque due to gas velocity gradient and was calculated as :

$$M_D = C_T \frac{1}{2} \rho \frac{d_p^5}{2^5} |\omega_r| \omega_r \quad (7)$$

Where ω_r is relative angular velocity and C_T denotes torque coefficient. The torque coefficient is a function of the Reynolds number that is based on relative angular velocity :

$$Re_{\omega_r} = \frac{\rho d_p \left| \frac{1}{2} \nabla \times u - \omega_p \right|}{\mu} \quad (8)$$

The torque coefficient was calculated using the equation given by [27]

$$C_T = \frac{128.64}{Re_{\omega_r}} (1 + 0.1005 \sqrt{Re_{\omega_r}}) \quad (9)$$

Drag force was given by [28] who formulated an expression that accounts for both the normal (n) and tangential (τ) components of the drag force.

$$F_D^{/} = \rho d_p u_n^{rel} \left(C_{D,n} u_n^{rel} \hat{n} + C_{D,\tau} u_\tau^{rel} \hat{\tau} \right) \quad (10)$$

where $\hat{n}$ and $\hat{\tau}$ are unit vectors in the normal and tangential direction, respectively.

The particle-wall interaction was formulated by adhesive force. This force was simulated by a constant adhesive force model that represents adhesion due to liquid bridge forces. This model utilizes a constant value of adhesive force that is a multiple of particle gravity force. The value of multiplication was rather large, 10^4, to mimic the same boundary condition as in the Lagrangian method.

After the particles were tracked through the airway replica, the deposition fraction was calculated. It is a ratio of particle amount deposited in a specific segment to the amount of particles entering the model and thus, represents a spatial distribution of deposited fibers.

3. Results

Calculated deposition fractions of carbon fibers are depicted in Fig. 2. Carbon fibers deposited primarily within the airway replica, in particular around bifurcations, and only approximately 15 % of fibers penetrated the replica and reached outlets toward the lobes.

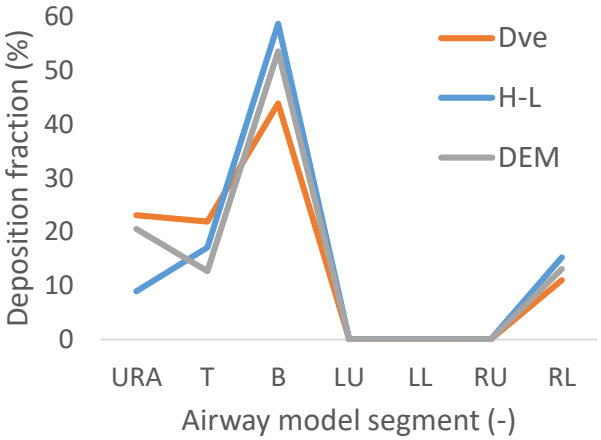

Fig. 2. Deposition fractions of carbon fibers in various airway model segments (URA – upper respiratory airways, T – trachea, B – bifurcations, LU – left upper lobe, LL – left lower lobe, RU – right upper lobe, RL – right lower lobe).

The high deposition fraction of carbon fibers was likely caused by their large dimensions, i.e. high inertia. Therefore, the fibers were not able to react to sudden changes of flow direction in the oropharynx, around vocal cords and around bifurcations, and collided with walls. Despite the high inertia, fibers reached the right lower lobe outlet (Fig. 3). This result originated in a more direct trajectory to right lower lobe compared to the other lobes.

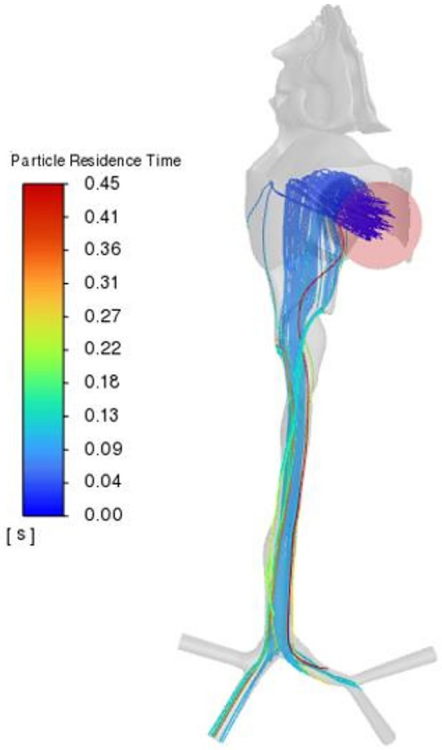

Fig. 3. Carbon fiber trajectories calculated by the H-L method.

The differences between the methods were not that significant. Generally, the volume equivalent method had the highest deposition fraction in the oral cavity and subsequently the lowest deposition fraction in the bifurcation region and outlets. The H–L method and DEM predicted that slightly more fibers penetrated the upper respiratory airways. DEM predicted that more fibers deposited in the upper respiratory airways and less in the trachea compared to H–L. This indicated that fibers simulated using DEM deposited in the bend of the oropharynx and around vocal cords while fibers simulated by the H–L method avoided more easily deposition in this region and deposited in the trachea.

Results of glass fiber deposition are depicted in Fig.4. The glass fiber deposition distribution differed from that of carbon fibers and high differences were found also between the methods. Volume equivalent sphere and H-L methods predicted that approximately 85 % of glass fibers penetrated the model, meanwhile DEM calculation showed that only roughly 54 % reached the outlets. Lower deposition compared to carbon fibers was expected as the dimensions of glass fibers were significantly lower than that of carbon fibers resulting in a lower effect of inertia [25].

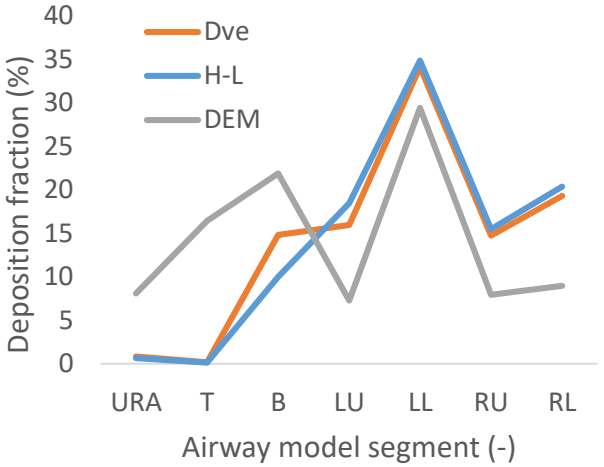

Fig. 4. Deposition fractions of glass fibers in various airway model segments (URA – upper respiratory airways, T – trachea, B – bifurcations, LU – left upper lobe, LL – left lower lobe, RU – right upper lobe, RL – right lower lobe).

The agreement between the methods was worse than in the case of carbon fibers. DEM predicted higher deposition inside the airway model and subsequently lower deposition at the outlets. This could be partly caused by the increased effect of interception. Fibers may come into contact with a wall and deposit because of their elongated shape even if their center of mass follows a streamline along the wall [29]. This effect is neglected in the Lagrangian method in which point particles with volume equivalent diameter are tracked. Concerning carbon fibers, the impact of interception could be diminished by the effect of inertia whose effect increases with increasing diameter. Moreover, the deposition of a fiber is compared to a spherical particle having a volume equivalent diameter. It may be more accurate to compare fiber with a spherical particle having the same aerodynamic diameter [30]. Carbon and glass fiber aerodynamic diameters based on equations given by [31] were 11.3 and 3.5 μm, respectively. Therefore, the deposition of glass fiber deposition could be

underestimated using volume equivalent diameter in the Lagrangian method.

4. Conclusions

Fiber deposition was investigated in a child airway replica that was created by downscaling an adult airway model. The replica consisted of upper respiratory airways and the tracheobronchial tree down to 2nd generation of branching. The model was employed in fiber deposition simulations using CFPD and CFD-DEM.

Carbon and glass fiber deposition was analyzed for stationary inhalation. The majority of carbon fibers were captured by the airway replica and only 15 % of fibers penetrated into one of the lobes. On the other hand, 85 % of glass fibers reached replica outlets and would continue deeper into child airways. These trends were caused by larger dimensions of carbon fibers compared to glass fibers and thus, the higher impact of the inertial deposition mechanism.

The volume equivalent diameter method overestimated the deposition in the replica for both carbon and glass fibers compared to the H-L method. DEM agreed reasonably well with the H-L method concerning carbon fibers but it predicted the highest deposition of glass fibers in the replica. This could be caused by the influence of the interception deposition mechanism that is neglected in both H-L and equivalent volume diameter methods. Another reason could be the use of equivalent volume instead of aerodynamic diameter.

Acknowledgement. This work was supported by the Czech Science Foundation under the grant GA22-20357S.

References

1 M. Belka, F. Lizal, J. Jedelsky, J. Elcner, P. K. Hopke, and M. Jicha, Journal of Aerosol Science **117**, 149 (2018).
2 N. D. Khoa, N. L. Phuong, K. Takahashi, and K. Ito, Jpn Archit Rev **5** (4), 592 (2022).
3 European Commission, The European Commission bans White Asbestos, 1999.
4 N. Alpert, M. van Gerwen, and E. Taioli, Transl Lung Cancer Res **9** (Suppl 1), S28 (2020).
5 M. D. Wright, A. J. Buckley, and R. Smith, Inhalation Toxicology **32** (7), 282 (2020).
6 K. Fujita, S. Obara, and J. Maru, Toxicology **466** (2022).
7 C. K. Zhang, L. C. Wu, M. de Perrot, and X. G. Zhao, Front Oncol **11** (2021).
8 W. Hofmann, Journal of Aerosol Science **42** (10), 693 (2011).
9 T. Myojo and M. Takaya, Ind Health **39** (2), 141 (2001).
10 Y. Zhou and Y. Cheng, in *Aerosol science and technology* (2005), Vol. 39, pp. 492.
11 W. C. Su and Y. S. Cheng, Journal of Aerosol Science **40** (3), 270 (2009).
12 Y. Feng and C. Kleinstreuer, Physics of Fluids **25** (9) (2013).
13 L. Tian and G. Ahmadi, Journal of Aerosol Science **60**, 1 (2013).
14 A. Farkas, F. Lizal, J. Elcner, J. Jedelsky, and M. Jicha, Journal of Aerosol Science **136**, 1 (2019).
15 A. Haider and O. Levenspiel, Powder Technol **58** (1), 63 (1989).
16 C. Kleinstreuer and Y. Feng, Journal of Biomechanical Engineering-Transactions of the Asme **135** (2) (2013).
17 F. G. Fan and G. Ahmadi, Journal of Aerosol Science **26** (5), 813 (1995).
18 L. Shachar-Berman, S. Bhardwaj, Y. Ostrovski, P. Das, P. Koullapis, S. Kassinos, and J. Sznitman, Pharmaceutics **12** (3) (2020).
19 R. X. Hu, Y. S. Liu, J. Ravnik, M. Hribersek, P. Steinmann, and Y. Cui, Comput Mech **69** (4), 1021 (2022).
20 F. Lizal, J. Elcner, P. K. Hopke, J. Jedelsky, and M. Jicha, Proceedings of the Institution of Mechanical Engineers Part H-Journal of Engineering in Medicine **226** (H3), 197 (2012).
21 L. Golshahi, M. L. Noga, R. B. Thompson, and W. H. Finlay, Journal of Aerosol Science **42** (7), 474 (2011).
22 M. H. Dave, M. Kemper, A. R. Schmidt, C. P. Both, and M. Weiss, Pediatr Anesth **29** (8), 782 (2019).
23 P. Koullapis, S. C. Kassinos, J. Muela, C. Perez-Segarra, J. Rigola, O. Lehmkuhl, Y. Cui, M. Sommerfeld, J. Elcner, M. Jicha, I. Saveljic, N. Filipovic, F. Lizal, and L. Nicolaou, European Journal of Pharmaceutical Sciences (2017).
24 M. Roy and C. Courtay, Radiation Protection Dosimetry **35** (3), 179 (1991).
25 W. C. Su and Y. S. Cheng, Journal of Aerosol Science **37** (11), 1429 (2006).
26 S. A. Morsi and A. J. Alexander, Journal of Fluid Mechanics **55** (Sep26), 193 (1972).
27 S. C. R. Dennis, S. N. Singh, and D. B. Ingham, Journal of Fluid Mechanics **101** (Nov), 257 (1980).
28 N. Marheineke and R. Wegener, International Journal of Multiphase Flow **37** (2), 136 (2011).
29 C. Darquenne, J Aerosol Med Pulm D **25** (3), 140 (2012).
30 K. Inthavong, A. P. Mouritz, J. L. Dong, and J. Y. Tu, Journal of Aerosol Science **65**, 58 (2013).
31 W. Stöber, Assesment of Airborne Particles, 249 (1972).